PHYSICAL REVIEW B **94**, 041113(R) (2016)

# Intrinsic carrier scattering mechanism in anatase $TiO_2$ investigated by ultraviolet-pump terahertz-probe spectroscopy

Y. Matsui,[1] T. Terashige,[1] R. Uchida,[1] T. Miyamoto,[1] H. Yada,[1] H. Matsuzaki,[2] B.-S. Li,[3] A. Sawa,[4] and H. Okamoto[1]

[1]*Department of Advanced Materials Science, University of Tokyo, Kashiwa, Chiba 277-8561, Japan*

[2]*Research Institute of Instrumentation Frontier, National Institute of Advanced Industrial Science and Technology (AIST), Tsukuba, Ibaraki 305-8568, Japan*

[3]*Academy of Fundamental and Interdisciplinary Sciences, Harbin Institute of Technology, Harbin City 150080, China*

[4]*Electronics and Photonics Research Institute, National Institute of Advanced Industrial Science and Technology (AIST), Tsukuba, Ibaraki 305-8562, Japan*

(Received 23 March 2015; revised manuscript received 4 March 2016; published 25 July 2016)

We measured the optical conductivity $\tilde{\sigma}(\omega)$ spectra caused by photocarriers in anatase $TiO_2$ by applying ultraviolet-pump terahertz-probe spectroscopy on epitaxially grown thin films. Drude model analyses of $\tilde{\sigma}(\omega)$ spectra reveal that, in the terahertz region, the reduced mass ($\hat{m}$) of the carriers is greater and their damping constant ($\gamma$) is smaller than those in the infrared region. With regard to the extended Drude model, these differences can be attributed to the frequency dependence of $\hat{m}$ and $\gamma$ originating from carrier-phonon scatterings. Furthermore, the interaction between carriers and Ti-O stretching modes in the 500–1000-$cm^{-1}$ region strongly influences the intrinsic carrier scattering mechanism in anatase $TiO_2$.

DOI: 10.1103/PhysRevB.94.041113

Titanium dioxide ($TiO_2$) is a promising material for applications in photocatalysis [1] and solar cells [2]. $TiO_2$ has three crystalline phases: anatase, rutile, and brookite. The anatase phase of $TiO_2$, shown in the inset of Fig. 1(a), is thermodynamically unstable in comparison with the other phases. However, the pulsed laser deposition (PLD) method enables us to obtain good-quality single-crystalline thin films of anatase $TiO_2$ [3]. In anatase $TiO_2$ films, electron doping is possible by substituting Ti with niobium (Nb) or tantalum [4–6]. Furthermore, the mobility of Nb-doped anatase $TiO_2$ exceeds 20 $cm^2\ V^{-1}\ s^{-1}$ at room temperature [4], which is higher than that in the rutile phase [7]. Optical spectroscopy from 0.2 to 1.2 eV on Nb-doped anatase $TiO_2$ reveals that doped carriers show Drude responses, and the electron effective mass $m_e$ is 0.2–0.6$m_0$ ($m_0$: the mass of electron) along the [100] direction [8]. More recently, pump-probe absorption spectroscopy from 0.1 to 2.0 eV has been performed on anatase $TiO_2$. Analyses of transient absorption spectra with the Drude model revealed that both electron carriers and hole carriers are mobile [9].

In order to consider potential applications of anatase $TiO_2$ in optoelectronic devices, the scattering mechanism of photocarriers (electrons and holes), which dominate carrier mobility, must be fully investigated. Transient terahertz (THz) spectroscopy is the most effective approach to accomplish this since responses in the terahertz region directly reflect the carrier transport mechanism as compared to those in the IR region. However, there are very few reports of such spectroscopy performed on anatase $TiO_2$.

Based on this information, in the present Rapid Communication, we measure the complex optical conductivity $\tilde{\sigma}(\omega)$ spectra due to photocarriers in anatase $TiO_2$ by transient terahertz spectroscopy. From analyses of the obtained $\tilde{\sigma}(\omega)$ spectra with the Drude model, we evaluate the reduced mass ($\hat{m}$) and damping constant ($\gamma$) of carriers in the terahertz region. The carrier scattering mechanism in anatase $TiO_2$ is described and clarified by comparing both the $\hat{m}$ and the $\gamma$ values in the terahertz region with those in the IR region.

An anatase $TiO_2$ epitaxial film fabricated on a $LaSrAlO_4$ (001) substrate using the PLD method is the sample used in this Rapid Communication. The quality of the film is verified with x-ray-diffraction measurements. The thickness of the film is about 100 nm. For the measurements of transient $\tilde{\sigma}(\omega)$ spectra, we perform ultraviolet-pump terahertz-probe spectroscopy [Fig. 1(b)]. A Ti-sapphire regenerative amplifier (RA) with a pulse width of ∼130 fs, photon (ph) energy of 1.55 eV, repetition rate of 1 kHz, and pulse energy of 0.8 mJ, is used as the light source. The output pulse from the RA is divided into two paths. One is used for the generation and detection of terahertz pulses. The other is used for the generation of ultraviolet-pump pulses with 4.65 eV. Terahertz pulses (0.7–2.7 THz) are generated by an air-plasma method [10] and detected by electro-optical sampling using a ZnTe crystal. Further details of the setup are described in the Supplemental Material [11]. The electric field of a terahertz pulse transmitted through the sample with [$E_{on}(t)$] and without the pump pulse [$E_{off}(t)$] is recorded.

In Fig. 1(c), the absorption coefficient ($\alpha_{TiO_2}$) spectrum of the anatase $TiO_2$ film is shown by the solid line, which is in good agreement with that previously reported (the broken line) [12]. The penetration depth $l_p(=1/\alpha_{TiO_2})$ of the pump light (4.65 eV) is 18 nm, which is sufficiently smaller than the film thickness (100 nm). Therefore, all of the pump light is absorbed in anatase $TiO_2$. Because of large absorption coefficients above 2.7 THz due to the $LaSrAlO_4$ substrate [13], the measureable frequency range is limited to 2.6 THz and below.

The solid line in Fig. 1(d) shows the time evolution in the photoinduced change $\Delta OD = -\log_{10}(1 + \Delta T_{TiO_2}/T_{TiO_2})$ of the optical density (OD), which is derived from the photoinduced change in the electric-field amplitude [$\Delta E(t) = E_{on}(t) - E_{off}(t)$] at the peak of the terahertz electric field. This ΔOD is roughly proportional to the change in transmissivity averaged from 0.7 to 2.6 THz. It increases

 

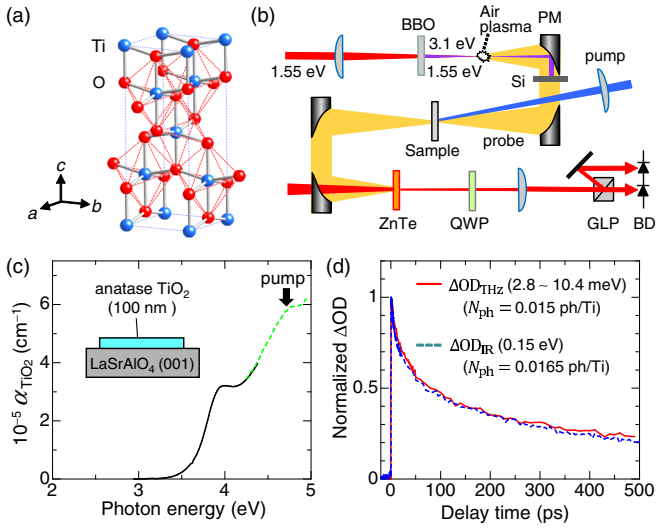


FIG. 1. (a) A crystal structure of anatase $TiO_2$. (b) Schematic of the ultraviolet-pump terahertz-probe spectroscopy $\beta$-$BaB_2O_4$ (BBO), off-axis parabolic mirror (PM), silicon wafer (Si), quarter-wave plate (QWP), Glan laser prism (GLP), and balanced detector (BD). (c) Absorption ($\alpha_{TiO_2}$) spectra of the anatase $TiO_2$ film measured in this Rapid Communication (solid line) and in a previous report (broken line [12]). (d) Time evolutions of photoinduced absorption changes in the terahertz region (2.8–10.4 meV) ($\Delta OD_{THz}$: solid line) and at 0.15 eV ($\Delta OD_{IR}$: broken line) [9].

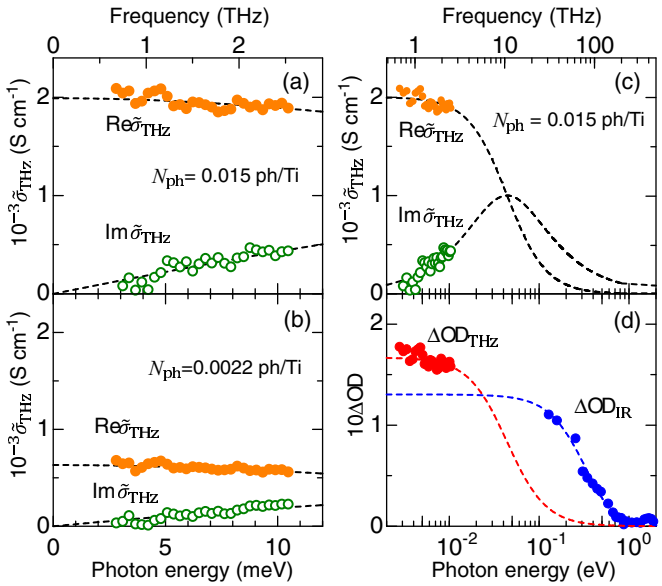


FIG. 2. (a) and (b) Transient Re $\tilde{\sigma}_{THz}(\omega)$ and Im $\tilde{\sigma}_{THz}(\omega)$ spectra at (a) $N_{ph} = 0.015$ ph/Ti and (b) $N_{ph} = 0.0022$ ph/Ti. (c) and (d) Logarithmic plots of (c) Re $\tilde{\sigma}_{THz}(\omega)$ and Im $\tilde{\sigma}_{THz}(\omega)$ and (d) $\Delta OD_{THz}$ ($N_{ph} = 0.015$ ph/Ti) and $\Delta OD_{IR}$ ($N_{ph} = 0.0165$ ph/Ti). Broken lines show fitting curves in the Drude model.

sharply within 0.2 ps after photoexcitation and decreases in a few hundreds of picoseconds. These changes are attributable to the generation and recombination of photocarriers. The observed dynamics is in good agreement with that for the IR (0.15-eV) probe previously measured in the similar excitation condition [9]. The analyses of $\Delta$OD in the IR region reveal that the relaxation process of the photocarriers is dominated by three-carrier Auger recombination [9]. Furthermore, the agreement of the $\Delta$OD dynamics between the terahertz and the IR regions means that absorption of the same photocarriers is detected as $\Delta$OD in both regions.

In order to measure the $\tilde{\sigma}(\omega)$ spectra due to the photocarriers in the terahertz region, we choose a delay time of 1 ps after the photoexcitation where photocarrier recombination is almost negligible. In the analysis, we assumed that the photoexcited $TiO_2$ film consists of two layers, the excited layer and the unexcited layer for simplicity. In this assumption, a metallic state with the thickness $l_p$ is initially formed from the surface of the $TiO_2$ film, and the carrier density is homogenous within the thickness $l_p$. The rest of the sample is unexcited. This assumption was used in the analysis of the photoinduced absorption spectra in the midinfrared to near-infrared region in the $TiO_2$ film [9]. On the basis of this assumption, we obtained $\tilde{\sigma}(\omega)$ spectra from the Fourier components $\tilde{E}_{on}(\omega)$ and $\tilde{E}_{off}(\omega)$ of $E_{on}(t)$ and $E_{off}(t)$, respectively, using the following equation [14,15]:

$$\tilde{\sigma}(\omega) = -\frac{\varepsilon_0 c(n+1)}{l_p}\frac{\Delta\tilde{E}(\omega)}{\tilde{E}_{off}(\omega)}, \quad (1)$$

where $\Delta\tilde{E}(\omega)$ is $\tilde{E}_{on}(\omega) - \tilde{E}_{off}(\omega)$, $\varepsilon_0$ is the permittivity of a vacuum, $c$ is the speed of light, and $n$ (= 6.71 [16]) is the refractive index of anatase $TiO_2$. Figures 2(a) and 2(b) show $\tilde{\sigma}(\omega)$ spectra for the photoexcitation densities of $N_{ph} = 0.015$ and 0.0022 ph/Ti, respectively. The calculation method of $N_{ph}$ is described in the Supplemental Material [11] where a free electron-hole pair is assumed to have been generated from one photon. With a decrease in frequency, the real part of $\tilde{\sigma}(\omega)$ [Re $\tilde{\sigma}(\omega)$] monotonically increases, whereas the imaginary part of $\tilde{\sigma}(\omega)$ [Im $\tilde{\sigma}(\omega)$] decreases [Figs. 2(a) and 2(b)]. We analyze these spectra with a two-carrier Drude model in which $\tilde{\sigma}(\omega)$ is expressed by the following equation:

$$\tilde{\sigma}(\omega) = \frac{N_{ph}e^2}{m_e}\frac{1}{\gamma_e - i\omega} + \frac{N_{ph}e^2}{m_h}\frac{1}{\gamma_h - i\omega}, \quad (2)$$

where $e$ is the electron charge, $m_e$ and $m_h$ are the effective masses of the electron and the hole, respectively, and $\gamma_e$ and $\gamma_h$ are the damping constants of the electron and the hole, respectively. Here, we assume $\gamma_e = \gamma_h (= \gamma)$ and introduce reduced mass $\hat{m} = m_e m_h/(m_e + m_h)$. Then, Eq. (2) is simplified to

$$\tilde{\sigma}(\omega) = \frac{N_{ph}e^2}{\hat{m}}\frac{1}{\gamma - i\omega}. \quad (3)$$

In this formula, the fitting parameters are $\hat{m}$ and $\gamma$. Hereafter, we discriminate parameters in the terahertz and IR regions by subscripts THz and IR, respectively.

The fitting results of Re $\tilde{\sigma}_{THz}(\omega)$ and Im $\tilde{\sigma}_{THz}(\omega)$ with Eq. (3) are indicated by broken lines in Figs. 2(a) and 2(b), which are good representations of the experimental data. In Fig. 2(c), the experimental and fitted curves are shown in a logarithmic plot of the photon energy. Although $\tilde{\sigma}_{THz}(\omega)$ data correspond to the low-frequency parts ($\omega < \gamma$) of

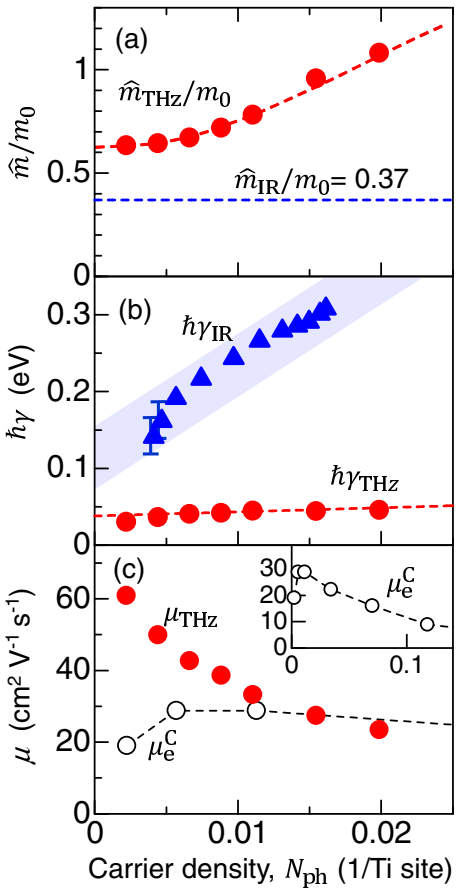


FIG. 3. (a)–(c) Carrier-density dependences of (a) $\hat{m}_{THz}/m_0$ and $\hat{m}_{IR}/m_0$, (b) $\hbar\gamma_{THz}$ and $\hbar\gamma_{IR}$, and (c) $\mu_{THz}$ and $\mu_e^C$ (the electron mobility in $Ti_{1-x}Nb_xO_2$ [5]).

the Drude dispersion, the parameters were uniquely determined because Re $\tilde{\sigma}_{THz}(\omega)$ and Im $\tilde{\sigma}_{THz}(\omega)$ are simultaneously fit. The parameters we obtain are $\hat{m}_{THz} = 0.96m_0$ and $\hbar\gamma_{THz} = 0.044$ eV for $N_{ph} = 0.015$ ph/Ti and $\hat{m}_{THz} = 0.63m_0$ and $\hbar\gamma_{THz} = 0.03$ eV for $N_{ph} = 0.0022$ ph/Ti. From $\hat{m}_{THz}$ and $\gamma_{THz}$, the mobility $\mu_{THz}[=\mu_{eTHz} + \mu_{hTHz} = e/(m_{eTHz}\gamma_{eTHz}) + e/(m_{hTHz}\gamma_{hTHz}) = e/(\hat{m}_{THz}\gamma_{THz})]$ is calculated to be 27 cm$^2$ V$^{-1}$ s$^{-1}$ for $N_{ph} = 0.015$ ph/Ti and 61 cm$^2$ V$^{-1}$ s$^{-1}$ for $N_{ph} = 0.0022$ ph/Ti. We analyze $\tilde{\sigma}_{THz}(\omega)$ spectra for various excitation densities in the same way and obtain excitation-density dependences of $\hat{m}_{THz}/m_0$, $\hbar\gamma_{THz}$, and $\mu_{THz}$ which are shown in Figs. 3(a)–3(c), respectively. We checked the validity of this analysis method by using two other analysis methods [11].

At low carrier densities, $\hat{m}_{THz}$ is equal to $0.62m_0$ [Fig. 3(a)], which is larger than the value ($\hat{m} = 0.46m_0$) evaluated from the band calculation ($m_e = 0.6m_0$ and $m_h = 1.9m_0$) [17]. The reason for the larger $\hat{m}_{THz}$ is discussed later. With an increase in $N_{ph}$, $\hat{m}_{THz}$ monotonically increases. This tendency was also observed in chemically doped samples [5] and can be explained by the anharmonic band dispersion [18]. $\gamma_{THz}$ exhibits a slight increase with an increase in $N_{ph}$ [Fig. 3(b)]. A similar tendency is reported from the analyses of $\tilde{\sigma}_{THz}(\omega)$ spectra in rutile $TiO_2$ and attributed to the increase in the Fermi velocity due to the increase in $N_{ph}$, which enhances the carrier-phonon scattering [19].

The decrease in $\hat{m}_{THz}$ and $\gamma_{THz}$ increases $\mu_{THz}$ as shown in Fig. 3(c). In the same figure, we show the values of the electron mobility $\mu_e^C$ determined from the transport measurement of electron-doped anatase $TiO_2$ ($Ti_{1-x}Nb_xO_2$) [5]. In the lower carrier-density range ($N_{ph} < 0.01$ ph/Ti), $\mu_{THz}$ is larger than $\mu_e^C$. This is significant although $\mu_{THz}$ includes the mobility of photoholes. Its contribution should be less than one-third of the mobility of photoelectrons due to the larger effective mass of holes [17]. However, in the lowest carrier density ($N_{ph} = 0.0022$ ph/Ti), $\mu_{THz}$ is more than twice as large as $\mu_e^C$. This cannot be explained by the hole mobility included in $\mu_{THz}$ and suggests that the introduction of Nb would increase extrinsic disorders, reducing $\mu_e^C$. On the other hand, at carrier densities higher than $N_{ph} = 0.015$ ph/Ti, $\mu_{THz}$ is slightly smaller than $\mu_e^C$. This is possibly due to the presence of electron-hole scatterings, increasing $\gamma_{THz}$.

Next, we compare optical responses in the terahertz and IR regions. In Fig. 2(d), we show $\Delta$OD spectra with the carrier densities 0.015 ph/Ti (THz) and 0.0165 ph/Ti (IR) together with the fitting curves in the Drude model (broken lines) [20]. Although the carrier densities are almost the same, the two fitting curves are significantly different. This spectral difference cannot be attributed to the difference in $N_{ph}$, suggesting that $\hat{m}$ and $\gamma$ actually depend on frequency. To ascertain this, we also plot the carrier-density dependence of $\hat{m}_{IR}/m_0$ and $\hbar\gamma_{IR}$ for the IR region [9] in Figs. 3(a) and 3(b), respectively. According to the previous report, $\hat{m}_{IR}$ is almost constant ($0.37m_0$) in this carrier-density region, whereas $\gamma_{IR}$ increases with increasing $N_{ph}$ [5,9]. Thus, the carrier-density dependencies of $\hat{m}_{IR}$ and $\gamma_{IR}$ are considerably different from those of $\hat{m}_{THz}$ and $\gamma_{THz}$.

To understand these discrepancies between $\hat{m}_{THz}(\gamma_{THz})$ and $\hat{m}_{IR}(\gamma_{IR})$, we use parameters for $N_{ph} \to 0$. In this limit, the $N_{ph}$ dependence of $\hat{m}$ and the effect of electron-hole scatterings in $\gamma$ can be neglected, and only electron-(hole-) phonon scatterings should be taken into account. In Figs. 4(c) and 4(d), we show with the shaded areas the values of $\hbar\gamma_{THz}(= 0.038$ eV), $\hbar\gamma_{IR}(= 0.11 \pm 0.04$ eV), $\hat{m}_{THz}(= 0.62m_0)$, and $\hat{m}_{IR}(= 0.37m_0)$ for $N_{ph} \to 0$ obtained from Figs. 3(a) and 3(b) [21].

To explain the results, we introduce the extended Drude model in which the dependences of $\hat{m}$ and $\gamma$ on frequency are taken into account. This model is widely used in simple metals [22], transition-metal compounds [23], heavy-electron systems [24], and high-$T_C$ cuprates [25,26]. When considering the frequency dependence of $\gamma$, $\gamma$ is expressed as $\tilde{\gamma}(\omega) = \gamma_1(\omega) + i\gamma_2(\omega)$. By introducing the renormalized Drude parameters $\gamma^*(\omega) = \gamma_1(\omega)/[1 + \lambda(\omega)]$ and $m^*(\omega) = \hat{m}[1 + \lambda(\omega)]$ with $\lambda(\omega) = \gamma_2(\omega)/\omega$, Eq. (2) is expressed as follows [26]:

$$\tilde{\sigma}(\omega) = \frac{N_{ph}e^2}{m^*(\omega)} \frac{1}{\gamma^*(\omega) - i\omega}. \quad (4)$$

Here, $\gamma_1(\omega)$ and $\lambda(\omega)$ are related to each other by the Kramers-Kronig relation,

$$\lambda(\omega) = \frac{2}{\pi} P \int d\Omega \frac{\gamma_1(\Omega)}{\Omega^2 - \omega^2}, \quad (5)$$

where $P$ denotes the Cauchy principal value.

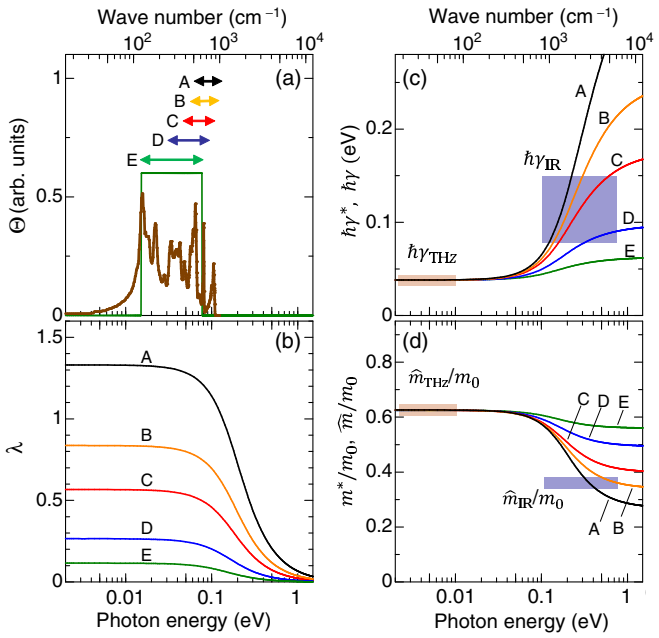


FIG. 4. (a) Phonon DOS evaluated by the first-principles calculation [29]. Arrows show energy regions A–E used for the calculation of $m^*(\omega)$ and $\gamma^*(\omega)$. In each region, the width is 0.062 eV, and a constant phonon DOS is assumed (A: 0.062–0.124 eV, B: 0.054–0.116 eV, C: 0.046–0.108 eV, D: 0.031–0.093 eV, and E: 0.015–0.077 eV). The thin solid line denotes a DOS for region E. (b) $\lambda(\omega)$ calculated for phonon DOSs of A–E. (c) $\gamma^*(\omega)$ calculated for photon DOSs of A–E. (d) $m^*(\omega)$ calculated for phonon DOSs of A–E. Shaded areas in (c) and (d) show the experimental $\hat{m}/m_0$ and $\hbar\gamma$ values.

Now, we can consider the carrier-phonon scattering in the extended Drude model [27,28]. When phonons contribute to carrier scattering processes, the frequency dependence of the damping constant is described by the following formula [27,28]:

$$\hbar\gamma_1(\omega) = \frac{\hbar\pi}{\omega}\int d\Omega\ \Theta(\Omega) \times\left[2\omega\coth\left(\frac{\hbar\Omega}{2k_BT}\right) - 2(\omega+\Omega)\coth\left(\frac{\hbar\omega+\hbar\Omega}{2k_BT}\right) + (\omega-\Omega)\coth\left(\frac{\hbar\omega-\hbar\Omega}{2k_BT}\right)\right]. \quad (6)$$

Here, $\Theta(\omega)$ represents the weighted density of states of phonons [27], and $T$ is the temperature, and $k_B$ is the Boltzmann constant. In anatase $TiO_2$, the phonon density of states (DOS) is derived by the first-principles calculation, which is shown in Fig. 4(a) (thick solid line) [29]. As in Ref. [25], we approximate $\Theta(\omega)$ using a constant DOS $\rho_0$,

$$\Theta(\omega) = \begin{cases} \rho_0 & (\omega_{\min} < \omega < \omega_{\max}), \\ 0 & (\omega \leqslant \omega_{\min} \text{ or } \omega_{\max} < \omega). \end{cases} \quad (7)$$

In order to simulate frequency dependence of $m^*(\omega)$ and $\gamma^*(\omega)$, we select five energy regions (A–E) with the widths of 0.062 eV indicated by arrows in Fig. 4(a) and assume that each region corresponds to $\omega_{\min} < \omega < \omega_{\max}$ and $\rho_0$ is constant. In this case, $\Theta(\omega)$ is rectangular as shown by the thin solid line in Fig. 4(a) for region E.

Using Eqs. (5)–(7), we can calculate $\lambda(\omega)$. In this calculation, we select the $\rho_0$ value for each region of phonon DOSs A–E so that $\hbar\gamma^*(\omega)$ is equal to the experimental value $\hbar\gamma_{THz} = 0.038$ eV at 1 THz. The resulting $\lambda(\omega)$ and $\hbar\gamma^*(\omega)$ are shown in Figs. 4(b) and 4(c), respectively. The five lines in these figures correspond to the five regions (A–E) indicated by arrows in Fig. 4(a). Using those $\lambda(\omega)$ values, we also calculate $m^*(\omega) = \hat{m}[1+\lambda(\omega)]$. We then select the $\hat{m}$ value which satisfies the condition that $m^*(\omega)$ is equal to $\hat{m}_{THz}(= 0.62m_0)$ at 1 THz. $m^*(\omega)$ obtained for A–E is shown in Fig. 4(d).

Figure 4(c) shows that $\gamma^*(\omega)$ increases after passing through the respective frequency region (A–E) where phonons are assumed to exist. This can be explained in the following way. In the case that a carrier's motion is perturbed by an electric field of light with a high frequency, the carrier obtains enough energy to excite a phonon through an inelastic scattering. This leads to the increase in $\gamma^*(\omega)$ in the energy region above the phonon energy, that is, the IR region. As seen in Fig. 4(d), $m^*(\omega)$ decreases in the energy region above the phonon energy. $\lambda(\omega)$ is related to $\gamma_1(\omega)$ via Eq. (5) such that $m^*(\omega)\{= \hat{m}[1+\lambda(\omega)]\}$ decreases in the region with higher energies than the phonon.

Finally, we discuss what kinds of phonons dominate the frequency dependence of $m^*(\omega)$ and $\gamma^*(\omega)$. Our approach is to compare the calculated values of $m^*(\omega)$ and $\gamma^*(\omega)$ with their experimental counterparts $\hat{m}_{IR}$ and $\hbar\gamma_{IR}$ in the IR region. Only the choice of region A can come close to reproducing both $\hat{m}_{IR}$ and $\hbar\gamma_{IR}$ in the IR region. This suggests that phonons in region A [0.062–0.124 eV (500−1000 cm$^{-1}$)] play important roles in carrier-phonon scatterings and dominate the frequency dependence of $m^*(\omega)$ and $\gamma^*(\omega)$ [30]. Details about the phonon modes in region A were reported previously [29,31] and are shown in the Supplemental Material [11]. All of the phonons in region A are classified as Ti-O bond-stretching-type vibrations, whereas phonons in the lower-frequency regions are O-Ti-O bond-bending-type vibrations [31]. This indicates that Ti-O bond-stretching-type vibrations especially contribute to the scattering of carriers.

To summarize, we measured optical conductivity spectra of the photocarriers in anatase $TiO_2$ by ultraviolet-pump terahertz-probe spectroscopy. From the fitting analyses of the obtained spectra with the Drude model, we evaluated the reduced mass and damping constant that depend on the photocarrier density. These parameter values were considerably different from those in the IR region. Such differences were attributed to the scattering of photocarriers by phonons of Ti-O bond-stretching-type modes. The experimental approach presented here should be effective for the understanding of carrier scattering mechanisms in various kinds of semiconductors.

This work was supported, in part, by a Grant-in-Aid by the Japan Society for the Promotion of Science (JSPS) (Grants No. 22740197 and No. 25247049).

Y. Matsui and T. Terashige contributed equally to this work.

[1] A. Fujishima and K. Honda, Nature (London) **238**, 37 (1972).

[2] B. O'Regan and M. Grätzel, Nature (London) **353**, 737 (1991).

[3] Y. Matsumoto, M. Murakami, Z. W. Jin, A. Nakayama, T. Yamaguchi, T. Ohmori, E. Suzuki, S. Nomura, M. Kawasaki, and H. Koinuma, Proc. SPIE **3941**, 19 (2000).

[4] Y. Furubayashi, T. Hitosugi, Y. Yamamoto, K. Inaba, G. Kinoda, Y. Hirosse, T. Shimada, and T. Hasegawa, Appl. Phys. Lett. **86**, 252101 (2005).

[5] Y. Furubayashi, N. Yamada, Y. Hirose, Y. Yamamoto, T. Hitosugi, T. Shimada, and T. Hasegawa, J. Appl. Phys. **101**, 093705 (2007).

[6] T. Hitosugi, Y. Furubayashi, A. Ueda, K. Itabashi, K. Inaba, Y. Hirose, G. Kinoda, Y. Yamamoto, T. Shimada, and T. Hasegawa, Jpn. J. Appl. Phys., Part 2 **44**, L1063 (2005).

[7] H. Tang, K. Prasad, R. Sanjines, P. E. Schmid, and F. Lévy, J. Appl. Phys. **75**, 2042 (1994).

[8] Y. Hirose, N. Yamada, S. Nakao, T. Hitosugi, T. Shimada, and T. Hasegawa, Phys. Rev. B **79**, 165108 (2009).

[9] H. Matsuzaki, Y. Matsui, R. Uchida, H. Yada, T. Terashige, B.-S. Li, A. Sawa, M. Kawasaki, Y. Tokura, and H. Okamoto, J. Appl. Phys. **115**, 053514 (2014).

[10] D. J. Cook and R. M. Hochstrasser, Opt. Lett. **25**, 1210 (2000).

[11] See Supplemental Material at http://link.aps.org/supplemental/10.1103/PhysRevB.94.041113, which includes Refs. [9,10,29,31], for the details of the optical-pump terahertz-probe spectroscopy, the evaluation method of the excitation density, the analysis methods of $\Delta\tilde{E}(\omega)/\tilde{E}_{\rm off}(\omega)$ spectra, and phonons in anatase $TiO_2$ in the range of $500-1000\,{\rm cm}^{-1}$.

[12] T. Fukumura, Y. Yamada, K. Tamura, K. Nakajima, T. Aoyama, A. Tsukazaki, M. Sumiya, S. Fuke, Y. Segawa, T. Chikyowa, T. Hasegawa, H. Koinuma, and M. Kawasaki, Jpn. J. Appl. Phys., Part 2 **42**, L105 (2003).

[13] T. Kiwa and M. Tonouchi, Jpn. J. Appl. Phys., Part 2 **40**, L38 (2001).

[14] H.-K. Nienhuys and V. Sundström, Phys. Rev. B **71**, 235110 (2005).

[15] The diffusion length of electron $\sqrt{\frac{k_{\rm B}T}{m_{\rm e}\gamma}t}$ along the perpendicular direction to the surface at 1 ps is estimated to be 6.1 nm, which is much smaller than the penetration depth ($l_{\rm p} = 18\,{\rm nm}$) of the pump pulse. Although the diffusion process cannot be completely neglected, the diffusion effect does not modify the main conclusion that the values of the parameters $\gamma$ and $m$ depend on the frequency since the diffusion process gives the similar effect on those parameters in two regions.

[16] R. J. Gonzalez, R. Zallen, and H. Berger, Phys. Rev. B **55**, 7014 (1997).

[17] L. Thulin and J. Guerra, Phys. Rev. B **77**, 195112 (2008).

[18] T. Pisarkiewicz, K. Zakrzewska, and E. Leja, Thin Solid Films **174**, 217 (1989).

[19] E. Hendry, M. Koeberg, J. Pijpers, and M. Bonn, Phys. Rev. B **75**, 233202 (2007).

[20] In order to make a reasonable comparison, we renormalized the $\Delta$OD of the infrared region. The carrier densities of the infrared and terahertz spectroscopies are similar to each other ($N_{\rm ph} = 0.015$ ph/Ti for THz and $N_{\rm ph} = 0.0165$ ph/Ti for IR). However, the excitation photon energy is different (4.0 eV for the infrared experiment and 4.65 eV for the terahertz experiment), which causes the difference in the penetration depth and thus the difference in the absolute value of $\Delta$OD.

[21] We set the energy width of the shaded areas for $\hat{m}_{\rm IR}$ and $\hbar\gamma_{\rm IR}$ considering that they were determined from the optical responses in the range of 0.1–0.7 eV [9].

[22] J. W. van der Eb, A. B. Kuz'menko, and D. van der Marel, Phys. Rev. Lett. **86**, 3407 (2001).

[23] J. W. Allen and J. C. Mikkelsen, Phys. Rev. B **15**, 2952 (1977).

[24] A. M. Awasthi, L. Degiorgi, G. Grüner, Y. Dalichaouch, and M. B. Maple, Phys. Rev. B **48**, 10692 (1993).

[25] A. V. Puchkov, D. N. Basov, and T. Timusk, J. Phys.: Condens. Matter **8**, 10049 (1996).

[26] D. N. Basov and T. Timusk, Rev. Mod. Phys. **77**, 721 (2005).

[27] P. B. Allen, Phys. Rev. B **3**, 305 (1971).

[28] S. V. Shulga, O. V. Dolgov, and E. G. Maksimov, Physica C **178**, 266 (1991).

[29] Z.-G. Mei, Y. Wang, S.-L. Shang, and Z.-K. Liu, Inorg. Chem. **50**, 6996 (2011).

[30] We confirmed that the calculation for a wide frequency region covering all phonons (0.015–0.124 eV) did not reproduce the experimental values.

[31] T. Ohsaka, F. Izumi, and Y. Fujiki, J. Raman Spectrosc. **7**, 321 (1978).